BRL-CR-690

AD-A250 758

(2)

CONTRACTOR REPORT BRL-CR-690

BRL

C

EXPERIMENTAL INVESTIGATION OF THE AXIAL IMPREGNATION OF ORIENTED FIBER BUNDLES BY CAPILLARY FORCES

ERDAL BAYRAMLI
MIDDLE EAST TECHNICAL UNIVERSITY

ROBERT L. POWELL
UNIVERSITY OF CALIFORNIA

DTIC
S ELECTE D
MAY 28 1992
B

MAY 1992

APPROVED FOR PUBLIC RELEASE; DISTRIBUTION IS UNLIMITED.

U.S. ARMY LABORATORY COMMAND

BALLISTIC RESEARCH LABORATORY
ABERDEEN PROVING GROUND, MARYLAND

92 5 27 065

92-13992

NOTICES

REPORT DOCUMENTATION PAGE

Form Approved
OMB No. 0704-0188

1. AGENCY USE ONLY *(Leave blank)*	**2. REPORT DATE** May 1992	**3. REPORT TYPE AND DATES COVERED** Final, Feb 1988-Mar 1990

4. TITLE AND SUBTITLE

Experimental Investigation of the Axial Impregnation of Oriented Fiber Bundles by Capillary Forces

5. FUNDING NUMBERS

PR: 1L162618AH80

6. AUTHOR(S)

Erdal Bayramli[a] and Robert L. Powell[b]

7. PERFORMING ORGANIZATION NAME(S) AND ADDRESS(ES)

[a]Department of Chemistry
Middle East Technical University
Ankara, Turkey

[b]Department of Chemical Engineering
University of California
Davis, California, USA

8. PERFORMING ORGANIZATION REPORT NUMBER

9. SPONSORING/MONITORING AGENCY NAME(S) AND ADDRESS(ES)

U.S. Army Ballistic Research Laboratory
ATTN: SLCBR-DD-T
Aberdeen Proving Ground, MD 21005-5066

10. SPONSORING/MONITORING AGENCY REPORT NUMBER

BRL-CR-690

11. SUPPLEMENTARY NOTES

Sponsored jointly by U.S. Army Ballistic Research Laboratory and Lawrence Livermore National Laboratory. Contracting Officer's Representative for this report is Dr. Bruce P. Burns, U.S. Army Ballistic Research Laboratory, ATTN: SLCBR-IB-M, Aberdeen Proving Ground, MD 21005-5066.

12a. DISTRIBUTION/AVAILABILITY STATEMENT

Approved for public release; distribution is unlimited.

12b. DISTRIBUTION CODE

13. ABSTRACT *(Maximum 200 words)*

Capillary impregnation of a viscous liquid into carbon fiber bundles is investigated experimentally. Axial impregnation is examined in which flow occurs primarily parallel to the fibers' axes. For silicone oils, as well as for a curing epoxy system, the kinetics of axial impregnation follow closely $h \alpha t^{1/2}$, where h is the average displacement of the advancing front and t is the time of impregnation. The impregnation rates are higher than those predicted by theoretical models based upon simple geometries. The rates are strongly influenced by the pore size distribution in the fiber bundles. At a given overall average porosity, higher rates of impregnation are observed for samples having a higher pore heterogeneity than those with a narrow distribution of pore sizes. An analysis of the experimental data is presented which allows the effective pore size distribution to be calculated.

14. SUBJECT TERMS

Carbon fibers, impregnation, porous materials, continuous fiber composites

15. NUMBER OF PAGES

39

16. PRICE CODE

17. SECURITY CLASSIFICATION OF REPORT	**18. SECURITY CLASSIFICATION OF THIS PAGE**	**19. SECURITY CLASSIFICATION OF ABSTRACT**	**20. LIMITATION OF ABSTRACT**
UNCLASSIFIED	UNCLASSIFIED	UNCLASSIFIED	SAR

INTENTIONALLY LEFT BLANK.

TABLE OF CONTENTS

INTENTIONALLY LEFT BLANK.

LIST OF FIGURES

INTENTIONALLY LEFT BLANK.

LIST OF TABLES

INTENTIONALLY LEFT BLANK.

ACKNOWLEDGMENT

This work was supported by a contract from Lawrence Livermore National Laboratory (LLNL). The encouragement of Dr. J. Lepper of LLNL is particularly appreciated.

INTENTIONALLY LEFT BLANK.

1. INTRODUCTION

The spontaneous penetration of liquids into porous materials under the influence of capillary forces is of importance in many physical and physiological processes. Understanding the basic mechanisms and relevant parameters associated with impregnation is required in fields as diverse as materials science and geology. Because of their widespread use in many advanced composite materials, we examine the impregnation of tows of carbon fibers. Our particular interest relates to the manufacturing of continuous fiber composite materials, wherein an essential unit process consists of impregnating bundles of dry fibers (a fiber tow) with a viscous resin. A typical carbon fiber tow is composed of 12,000 individual fibers (a 12K tow) having perimeters from 15 to 30 μm. The circumferences of the fibers we investigate are nearly circular. The tows constitute a simple model porous system of axially aligned rods and we consider impregnation driven solely by capillary forces.

In a regular array of parallel fibers, two types of flow can be envisaged: axial flow along the fiber axis and transverse (normal) flow normal to the axes of the fibers. In a perfectly regular lattice structure of fibers (e.g., hexagonally packed), axial penetration occurs if the fibers touch with their axes normal to the liquid surface. Normal impregnation takes place if the fibers touch with their axes parallel to the liquid surface. In many cases of practical importance both modes of impregnation co-exist due to (1) the irregularities in the lattice structure and (2) the application of liquid in an arbitrary direction. However, in processes associated with the manufacture of continuous fiber composites, the normal impregnation mode dominates. The adhesive is applied to the surface of a continuous tow and impregnation occurs by a combination of capillary forces and applied pressure.

In a previous publication (Bayramli and Powell 1990), we studied normal impregnation theoretically and predicted rates 10 to 100 times slower compared with axial impregnation as described by the Lucas-Washburn approximation (Lucas 1918; Washburn 1921). An experimental study of normal impregnation has provided qualitative confirmation of these theoretical predictions (Bayramli and Powell, to be published).

In this study, we investigate axial impregnation experimentally and compare the results with the theoretically predicted rates of wicking in a hexagonally packed regular array of fibers. For all data reported, the capillary number (ratio of the surface to gravitational forces) is sufficiently large (> 10^3) so that surface tension forces dominate. A novel analysis of the data permits the calculation of the effective pore size and the pore size distribution in the fiber tows.

2. THEORETICAL BACKGROUND

We investigate flow in a porous medium which has a constant cross-sectional geometry normal to the direction of flow. Figure 1 shows such an array, with the flow occurring normal to the plane of the figure (i.e., along the fibers' axes). It is assumed that the fluid is linearly viscous (with viscosity μ), that inertial and gravitational effects can be neglected, and that the flow is driven solely by capillary forces. If at $t = 0$ impregnation commences, then the distance of impregnation of the liquid into the medium, h, is given by Lucas (1918) and Washburn (1921),

$$h = At^{1/2} \tag{1}$$

$$A = A' (\gamma \cos \theta/\mu)^{1/2} \tag{2}$$

where A' is a constant which basically depends upon the geometry of the medium, γ is the surface tension, and θ is the apparent contact angle of the contact line on the solid wall.

For simple models of porosity, it is possible to determine the functional form of A'. For example, if the interstices of the medium consist of uniform hollow cylinders with radius r, then

$$A' = (r/2)^{1/2} \ . \tag{3}$$

If the geometry is more complicated (e.g., a regular hexagonal packing of axially oriented solid cylinders, where the flow occurs in the pores between the cylinders), the calculations are cumbersome. Not only is the pressure jump across the interface hard to calculate because of its complicated shape, but also the solution of the creeping flow equations is difficult due to the geometrically complex boundary conditions.

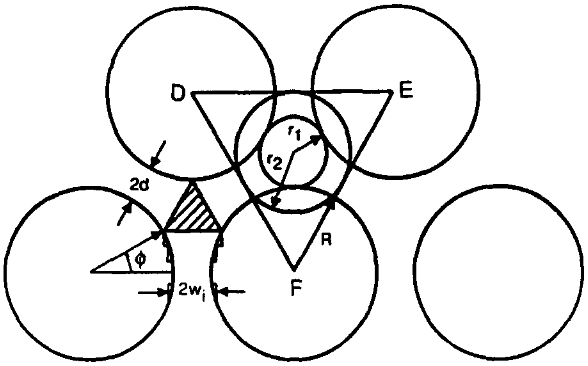

Note: The r_1 and r_2 denote the Radii of two imaginary capillaries and $2d$ is the minimum fiber-to-fiber spacing. Parallel plates extend along the fiber's axis and the body angle ϕ is increased in such a way as to compensate one-third of the volume of the shaded area (Bayramli and Powell 1990). The other two-thirds is compensated by the neighboring two pores.

Figure 1. Regular Hexagonal Packing of Fiber.

It is possible to calculate the constant A' as a function of porosity for various pore geometry approximations of the regular hexagonal packing of fibers shown in Figure 1. The porosity P is calculated for the unit triangular cell DEF in Figure 1 as

$$P = 1 - \frac{\pi}{(2\sqrt{3})\ [1 + (d/R)]^2} \tag{4a}$$

where R is the fiber radius and $2d$ is the minimum fiber-to-fiber separation.

If the impregnation dynamics are approximated by assuming that wicking occurs in a series of hollow cylinders between the fibers, impregnation rates A_1 and A_2 corresponding to r_1 and r_2 (Figure 1) can be calculated. For these simple geometries, the imaginary cylindrical capillaries with radii r_1 and r_2 can be related to P as follows:

$$r_1 = \frac{[\pi R^2/2\sqrt{3}(1 - P)]^{1/2}}{\cos\pi/6} - R \tag{4b}$$

$$r_2 = \tan\frac{\pi}{6}\left[\frac{\pi R^2}{2\sqrt{3}\,(1 - P)}\right]^{1/2} \quad . \tag{4c}$$

The rate A is then calculated as a function of porosity using Equations 4a, 4b, and 4c and substituting into Equations 1 and 3, noting that both r_1 and r_2 are uniquely determined by d.

It is most useful to express our experimental results as well as the model predictions in dimensionless terms. Expressed nondimensionally, Equation 1 is

$$\bar{h} = \bar{A}\,\bar{t}^{\,1/2} \tag{5}$$

where the bars denote nondimensional quantities which are defined as

$$\bar{h} = \frac{h}{R} \quad , \quad \bar{r} = \frac{r}{R} \quad , \quad \bar{t} = \frac{\gamma\cos\theta}{\mu R}t \quad .$$

The parameter $\bar{A}$ can be calculated using a model which divides the fiber perimeter into parallel plates extending along the fiber axis, as shown in Figure 1. By this method, we can make use of the actual capillary pressure for hexagonal packing derived by Princen (1969), rather than using the cylindrical pore approximation. The viscous resistance is calculated by dividing the fibers' surfaces into small parallel plates extending along the axes of the fibers. The excess shaded triangular area in Figure 1 can be incorporated into the parallel plate approximation by increasing the body angle ϕ slightly so that all the pore area is taken into account. For pressure driven flow along the parallel plates, the flow rate depends on the cube of the separation of the plates, $2w$. Therefore a flow average separation, $2w_{ef}$, can be defined as

$$2w_{ef} = \left[\frac{1}{n}\sum_{i=1}^{n}(2w_i)^3\right]^{1/3} \tag{6}$$

where n is the number of parallel channels which follow the contour of the fiber perimeter closely (an arbitrarily large number chosen to be 1,000). For the triangular unit cell in Figure 2, DEF, Princen (1969) defined the upward surface tension force for porosities above 0.20 for $\theta = 0°$ C and above 0.153 for $\theta = 60°$. From his results, the capillary pressure (Δp) for the hexagonal geometry can be easily obtained by dividing it by the pore area over which it acts:

$$\Delta p = \frac{\pi\gamma\cos\theta}{R[(1+\bar{d})^2\sqrt{3} - \pi/2]} \tag{7}$$

where $\bar{d} = d/R$. Substituting Δp from Equation 7 into the Lucas-Washburn type creeping flow equation for the parallel plate approximation of the hexagonal fiber packing, we find

$$\bar{A}_{hp} = 2\bar{w}_{ef}\left[\frac{\pi\cos\theta}{6(1+\bar{d})^2\sqrt{3} - \pi/2}\right]^{1/2} . \tag{8}$$

Here $\bar{w}_{ef} = w_{ef}/R$ and $\bar{A}_{hp}$ is the impregnation constant for the hexagonally packed regular fiber structure appearing in an appropriately dimensionless form of Equation 5.

The theoretical impregnation rates for fiber bundles having various porosities as a function of $\bar{A}_1$, $\bar{A}_2$, $\bar{A}_{hp}$ are compared with the experimental results in Section 4.

3. EXPERIMENTAL

3.1 <u>Materials</u>. The mass of liquid impregnated into axially oriented carbon fiber tows is measured by suspending the tow from an electrobalance with the fibers' axes aligned with gravity. The electrobalance is a Cahn R100 which can measure to 1 µg and is stable at 10 µg up to one day. A beaker containing the liquid is placed on a movable stage. The beaker is raised until the surface of the liquid touches the tow and forms a meniscus around it (Figure 2a). All experiments reported here were conducted at room temperature. The carbon fiber samples for the impregnation studies are prepared by placing a 0.4-m-long tow under tension and applying adhesive tape tightly to both sides of the tow in a

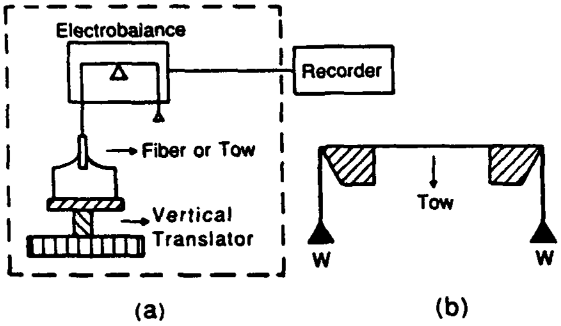

Note: (a) Tow impregnation and single-fiber experiments, and (b) the preparation of tow samples under tension. *W* is 0.239 kg.

Figure 2. Schematic Diagram of the Experimental Setup.

way that encapsulates it (Figure 2b). The strip is then cut into pieces 20–40 mm long, and each of these is trimmed on the sides to be used in an impregnation experiment. The taping process produces a controlled volume and gives rigidity to the sample. It can be suspended from one of the arms of the electrobalance through a small hole drilled in the sample. The liquid enters the sample only through the bottom cross-sectional surface located at the hydrostatic zero level. A blank test made by adhering two tapes face-to-face and trimming down to sample size showed no impregnation. Further, the interference of the adhesive tape with the surface tension measurement can be neglected, and the contact angle of the silicone oil on carbon fiber can be taken to be zero. For the epoxy system, a certain amount of contamination is possible through dissolution of the adhesive on the tape. However, no change in the measured wetting force of the epoxy system was observed when it was in contact with the adhesive tape. Lastly, the ratio of the carbon fiber surface area inside the sample compared with the surface area of the enclosing tape is about 25/1. Therefore, depending on the contact angle of the liquid on the tape, it can introduce a maximum of 4% error in the measurements.

The carbon fibers are available as continuous 12K tows. The particular fibers and their suppliers are listed in Table 1. All results reported here are for sized fibers. The perimeters of single carbon fibers are measured by the fiber balance wetting technique, which has now become a standard way to characterize single fibers (Okagawa and Mason 1978). For this purpose, hexadecane is used as the wetting liquid, which gives a nearly zero contact angle with carbon fibers. The experimental setup is essentially the same as that used for the impregnation studies and is shown schematically in Figure 2. Contact angles of the

Table 1. Properties of the Fibers and Liquids

CARBON FIBER	Perimeter[a] (μm)	Density (kg m^{-3})	
IM7 (Hercules)	15.7	1,870	
T-1000B (Torayca)	21.6	1,610	
Magnamite AS4 (Hercules)	25.1	1,770	
Celion G30-500 (BASF)	21.2	1,780	
LIQUID	Viscosity (Pa s)	Density (kg m^{-3})	Surface Tension (mN m^{-1})
Silicone oil[b] (10 cs)	0.102	940	20.1
Silicone oil[b] (100 cs)	0.93	968	20.6
Silicone oil[b] (500 cs)	4.75	972	21.1
Hexadecane		773	25.7
Adhesive[c,d]	13.4	1,102	35.3

[a] Average value.

[b] Dow Corning 200 fluids; values at 25° C.

[c] 100/40 (w/w) Epoxy (bisphenol-A-di-glycidyl ether)/hardener (aliphatic polyethertriamine).

[d] Viscosity, density, and surface tension of the epoxy system are about constant for 3 hours after mixing.

epoxy system with the carbon fibers are determined from the perimeter measurements and the total wetting force on single fibers.

The densities of the carbon fibers are determined using a pycnometer. A 1-m-long tow is cut into 2-mm-long strips and completely wetted in hexadecane. From the weight of the pycnometer with hexadecane, and with hexadecane plus carbon fiber, the density of the carbon fibers can be calculated. The weight per unit length of a tow is measured by applying the same tension as that used in the preparation samples for the impregnation studies to a nominally 1-m-long tow and measuring the exact length and weight of the tow.

The epoxy system is bisphenol-A-di-glycidyl ether (Der 332, Dow Chemicals) and an aliphatic polyethertriamine (Jeffamine T403, Jefferson) at 100/40 (w/w) epoxy/hardener ratio. It is degassed at 0.35 atm after mixing, and a profuse amount of bubble formation is observed which lasts about 15 min. In addition to the epoxy, various silicone fluids were used (Table 1). The surface tension of the liquids used in the experiments is determined by the Wilhelmy Plate technique and the viscosities are measured using a Visco-electric Analyzer (Sangamo-Schlumberger, Bognor Regis, U.K.).

Cross-sectional views of the epoxy impregnated and cured tows are obtained by optical reflectance and scanning electron microscopies. The surfaces of the samples are prepared by diamond polishing.

3.2 Analysis. The result of a typical experiment is given in Figure 3 where the nondimensional volume $\bar{V} = V/R^3$ (V being the instantaneous volume of liquid impregnated) is shown as a function of the square root of the dimensionless time $\bar{t}$. In this and subsequent figures, $\bar{V}$ is calculated by dividing the measured mass by density. The volume increases linearly with $\bar{t}^{1/2}$. Towards the end of the experiment, there is deviation from linearity, indicating that the impregnation front in the tow is irregular. Capillaries with different pore dimensions have different wicking rates. There is attrition as those with the large diameters (with higher rates of impregnation) are completely filled while flow continues in pores of smaller dimensions. The net effect is to decrease the overall rate of impregnation. We note that nonlinear behavior may result also from levelling off as the equilibrium capillary height is approached. In these experiments, the samples are sufficiently short so that such effects are not present.

This finding is further supported by the studies using epoxy. The epoxy system used in these experiments has a long pot life with its room temperature viscosity staying practically unchanged for 3 hours after mixing (Morgan, Kong, and Walkup 1984). Before it hardens completely, the maximum distance the curing epoxy system can axially impregnate into a carbon fiber tow is about 40 mm, depending on the type and the porosity of the tow. An examination of the hardened cross sections of epoxy-impregnated tows near the leading edge of the meniscus reveals a penetration difference of as much as 4 mm in various pores of the samples. It is, therefore, not possible to relate accurately the volume increase in the linear part of Figure 3 to a unique contact line displacement. However, an estimate of the overall wicking rate can be obtained from the slope of the linear region of the impregnation curve.

It is not possible to determine the initial point on the curve in Figure 3 by subtracting the external meniscus force from the total measured force. This results from the meniscus force being large with respect to the weight of the liquid inside the tow at early times, and from the inaccuracy in the determination of the external perimeter of the tow sample. The initial point shown in Figure 3 ($\bar{t} = 0$, $\bar{V} = 0$) is calculated by extrapolating the measured volume, after the formation of the meniscus, back to $t = 0$ assuming a linear $\bar{V}$ *vs.* $\bar{t}^{1/2}$ relationship. If the linearity assumption were not valid, the straight line would not pass through subsequent data points, which is found to be the case in all experiments.

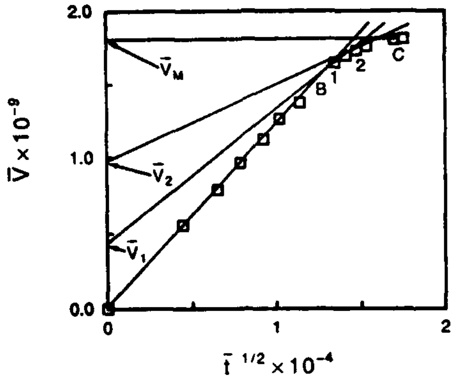

Note: Using Equation 9, the porosity is calculated to be 0.588. The slopes at points 1 and 2 are for illustration purposes and show $\bar{V}_i$, from which the pore size distribution is calculated. The maximum amount of liquid volume impregnated is $\bar{V}_M$.

Figure 3. Impregnation Curve of a 40-cm-Long IM7 Carbon Tow With 100 cs Silicone Oil.

The porosity of the tow can be calculated from the maximum volume of liquid impregnated (V_M), the length of the tow (L), the density of the carbon fibers (ρ_F), and the mass per unit length of the tow (M_T) using

$$P = \frac{\rho_F V_M}{\rho_F V_M + L M_T} \quad . \tag{9}$$

The experimental rate of impregnation can be calculated approximately from the linear portion of Figure 3, assuming the front advances smoothly with $h/L = V/V_M$. A more accurate experimental rate is calculated by making use of the nonlinear portion of Figure 3. If the lateral motion of the liquid in the tow is ignored, the fiber bundle can be visualized as a collection of individual capillaries with a distribution of pore sizes. The volume of liquid impregnated to a maximum distance h_M within pores that have characteristic dimensions between r and $r + \Delta r$ is determined by extrapolating the tangent of the $\bar{V}$ *vs.* $\bar{t}^{\,1/2}$ curve back $\bar{t} = 0$.

To prove this, let $N(\bar{V})$ denote the number of pores having volume $\bar{V}$, and $\bar{V}_M$ be the largest pore volume. As time progresses, the larger pores tend to fill first. The total volume of liquid in a sample, $\bar{V}_T$, is given by

$$\bar{V}_T(t) = \int_0^{\bar{V}_1(t)} N(\bar{V})d\bar{V} + \int_{\bar{V}_1(t)}^{\bar{V}_M} N(\bar{V})d\bar{V} \quad . \tag{10}$$

In Equation 10, the second term accounts for the volume in those capillaries which have completely filled at time t, while the volume contribution from the first term is from capillaries in which liquid is still flowing, with $\bar{V}_1(t)$ being the largest capillary in which there is flow. We consider our volumes as being composed of a series of capillaries, for which by Equations 1–3, when flow occurs

$$\bar{V} = \pi\bar{r}^{5/2}\bar{t}^{1/2} \tag{11}$$

$$d\bar{V} = \frac{5}{2}\pi\bar{r}^{3/2}\bar{t}^{1/2}d\bar{r} \quad . \tag{12}$$

Substituting Equation 12 into Equation 10,

$$\bar{V}_T(t) = \frac{5}{2}\pi\left\{\int_0^{\bar{r}_1(t)} N(\bar{r})\bar{r}^{3/2}\bar{t}^{1/2}d\bar{r} + \int_{\bar{r}_1(t)}^{\bar{r}_m} N(\bar{r})\bar{h}_m 2\pi\bar{r}d\bar{r}\right\} \tag{13}$$

where $\bar{r}_1(t)$ is the largest pore radius being filled at time $\bar{t}$, and $\bar{r}_m$ is the maximum pore radius in a sample. Differentiating Equation 13 with respect to $\bar{t}^{1/2}$ and applying the Leibniz rule

$$\frac{d\bar{V}_T}{d\bar{t}^{1/2}} = \frac{5}{2}\pi\int_0^{\bar{r}_1(t)} N(\bar{r})\bar{r}^{3/2}d\bar{r} \quad . \tag{14}$$

Equation 14 is the tangent to the $\bar{V}_T$ *vs.* $\bar{t}^{1/2}$ curve. Extrapolating the tangent back to $\bar{t}^{1/2} = 0$ and letting $\bar{V}_i(t)$ be the intercept, a comparison of the integrated form of Equation 13 and Equation 14 gives

$$\bar{V}_i = 2\pi \bar{h}_m \int_{\bar{r}_1(t)}^{\bar{r}_m} \bar{r} N(\bar{r}) d\bar{r} \quad . \tag{15}$$

This is simply the contribution of completely filled capillaries to the overall volume $\bar{V}_T$ at time $\bar{t}$.

To calculate a pore size distribution, we consider two intercepts, $\bar{V}_{i-1}$ and $\bar{V}_i$, with $\Delta\bar{V}_i = \bar{V}_i - \bar{V}_{i-1}$. Letting $N_i = N(r_i)$ be the number of pores having volumes between $\bar{V}_{i-1}$ and $\bar{V}_i$, and employing Equation 15, we have

$$N_i = \frac{\Delta\bar{V}_i}{\pi\bar{r}_i^2 h_m} \tag{16}$$

where $\bar{r}_i$ is the mean radius of the capillaries having volume $\Delta\bar{V}_i$. To use Equation 16, we begin by calculating $N(r_i)$ at the time when all the capillaries are full, $t \to \infty$. At regular $\bar{t}^{1/2}$ intervals, slopes are taken and extrapolated to $\bar{t}^{1/2} = 0$. The first non-zero slope belongs to an average of the smallest capillaries when all the other larger capillaries are full; therefore, it represents a rate which is solely due to the smallest capillaries. The first $(V_M - V_i)$ gives the volume of these small pores. Subsequent slopes and the volume increments belong to progressively larger pores and, hence, independent contributions $(V_i - V_{i-1})$ of all individual mean capillaries to the maximum volume, V_M, can be determined. The number of capillaries can then be calculated from Equation 16 employing the rate relationships given in Equations 1–3 for the case of cylindrical geometry. For an accurate extrapolation of the tangents in the nonlinear part of the curve back to the $\bar{V}$ axis, a smoothing of the data is performed using a polynomial approximation of the curve. It is found that a fourth-order polynominal fits the nonlinear data points and, therefore, an accurate extrapolation of the data points to the volume axis can be made. We have divided the nonlinear portion of the curve from B to C into 50 equal $\bar{t}^{1/2}$ increments and obtained 50 extrapolated values of V_i such that the total volume impregnated at long times, $\bar{V}_T(\infty)$, is given by

$$\bar{V}_T(\infty) = \sum_{i=1}^{50} \Delta \bar{V}_i \quad . \tag{17}$$

The entire curve part in Figure 3 from B to C is used to calculate an average experimental impregnation constant $\bar{A}$ as follows:

$$\bar{A} = \sum_{i=1}^{50} \bar{A}_i \frac{\Delta \bar{V}_i}{\bar{V}_m} \quad . \tag{18}$$

It should be noted that no assumption as to the pore geometry is required to find $\bar{A}$ experimentally, but to compare with theory, a model pore geometry must be assumed.

4. RESULTS AND DISCUSSION

Among the carbon fibers used the IM7 has the most regular and round cross section (Figure 4). We have used silicone liquids, which have contact angles of approximately zero on carbon fibers, to determine the kinetics of axial impregnation into IM7 fiber bundles. Representative results are summarized in Table 2. The porosities in experiments 1–9 varied from 49.65 to 59.60. The experimental values of $\bar{A}$ calculated from the linear and the nonlinear portions of the impregnation curve differed slightly. Therefore, a good approximation can be achieved by using $\bar{h}$ *vs.* $\bar{t}^{\,1/2}$ of the linear part in the kinetic relationships. The data in Table 2 demonstrate that $\bar{A}$ is not simply a function of the porosity, as defined by Equation 9. Similar porosities in experiments 4–7 of about 0.57 give rise to very different rates of impregnation. The effective radius $\bar{R}_{avg}$, which corresponds to $\bar{A}$ as calculated using Equations 1–3, shows a much larger standard deviation σ_R in experiments with faster rates.

Figure 5 shows the wicking curves for four experiments using carbon fiber tows having about the same porosity. It is possible to observe a more gradual transition from linear to nonlinear regimes of impregnation in the faster experiments. The experiments with faster rates showed a second-order transition

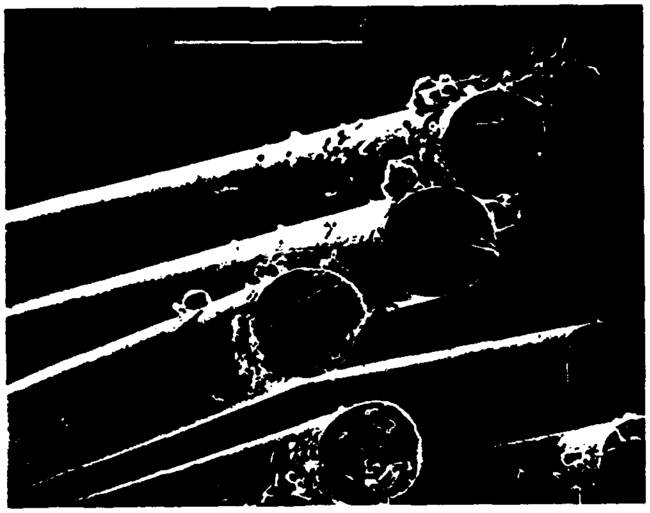

Note: The bar denotes 10 μm.

Figure 4. Scanning Electron Micrograph of the IM7 Carbon Fibers.

Table 2. Analysis of the Data for IM7 Carbon Fibers

Experiment	Porosity[a]	Liquid[b] Viscosity	$\bar{A}$	$\bar{A}$	$\bar{R}_{avg}$ [c]	σ_R [d]
			Nonlinear	Linear		
1	49.6	500	0.88	0.91	1.55	0.29
2	50.2	100	0.89	0.95	1.58	0.33
3	51.1	500	0.98	0.99	1.91	0.37
4	56.8	100	1.08	1.14	2.32	0.55
5	57.0	10	1.46	1.52	4.24	1.25
6	57.3	500	1.88	1.88	7.10	2.76
7	57.5	10	0.89	0.95	1.58	0.33
8	58.8	100	1.16	1.21	2.70	0.49
9	59.6	500	1.12	1.07	2.51	0.58

Note: The impregnation constants $\bar{A}$ that are calculated using Equation 19 are denoted $\bar{A}$ (nonlinear) and the slope of the linear portion of $\bar{h}$ *vs.* $\bar{t}^{1/2}$ is $\bar{A}$ (linear)

[a] Equation 9.

[b] As cited by the manufacturer.

[c] Weighted average of the radii calculated from the non-linear portion of $\bar{V}$ *vs.* $\bar{t}^{1/2}$, $(1/n)$

$$\left(\sum_{i=1}^{n} N(R_i)\,(\bar{R}_i)^2 \right)^{1/2} .$$

[d] Standard deviation of $\bar{R}_{avg}$ calculated from the distribution of radii in a given experiment.

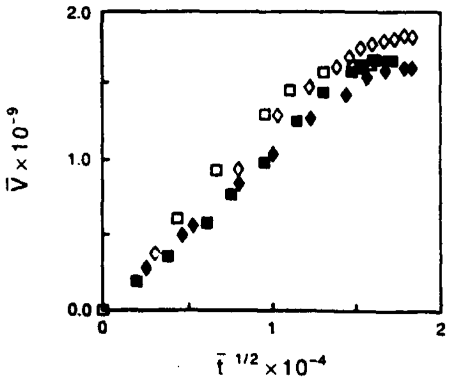

Note: See Table 2: ◇, Experiment 4; □, Experiment 5; ■, Experiment 7; ◆, Experiment 9.

Figure 5. Impregnation Curves for Experiments 4, 5, 7, and 9.

from linear to nonlinear behavior as compared with those having slower rates. In the latter case, the transition was closer to being first-order, indicating that all portions of the advancing contact line reach the top of the sample at roughly the same time. The pore size distributions calculated using Equation 16 for three of the sets of data in Figure 5 are given in Figure 6. The fastest rate is for experiment 5 where the pore size distribution is the widest and σ_R is the largest. These data also allow us to calculate the capillary number (*Ca*) and thereby test our assertion that gravitational forces are negligible relative to surface tension forces. Letting $Ca = 2\gamma/\rho rhg$, where g is the gravitational acceleration, we find that for a tow having a 50% porosity, the average pore radius is $4 \cdot 10^{-3}$ mm, leading to $Ca = 2 \cdot 10^{5}$. Even for the largest pore diameters suggested by the distributions in Figure 6, $r = 20$ μm and $Ca = 2 \cdot 10^{3}$.

When silicone fluids are used for the impregnation experiments, the initial linear relationship between $\bar{V}$ and $\bar{t}^{\,1/2}$ is valid for all the carbon fibers investigated in this study, as seen from the representative data in Figures 7 and 8. For the epoxy system, the nondimensional data corrected for non-zero contact angle also show linearity for G30-500 and T-1000B fiber tows in the initial stages of cross-linking (curing). A slight curing effect is noticeable for both sets of epoxy data at long times. The linearity simply implies that the average cross-sectional geometry in a given tow is constant, although it is not possible to determine the dependency of the slope upon the geometry without a theory of impregnation. It is also not warranted to compare systems with different contact angles in cases where normal impregnation may occur due to the strong dependence of normal impregnation kinetics on contact angle (Bayramli and Powell 1990).

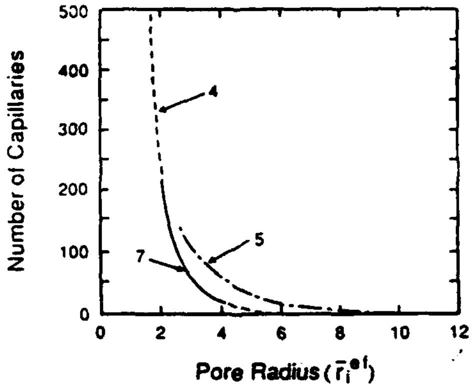

Note: *This is assuming the Radii are discretely distributed over 50 values, for three different experiments using tows of similar porosities. The experiment numbers are indicated on the curves.*

Figure 6. Distribution of the Effective Pore Radii.

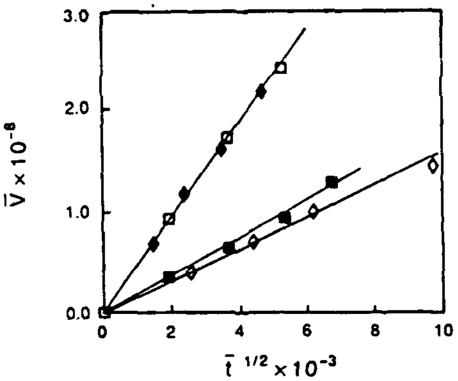

Note: Experiments 19 (◇), 24(□), 26 (◆) (θ = 0°), and the epoxy adhesive (■), (θ ≈ 32°). (Contact angle normalization is applied to the epoxy data.)

Figure 7. Linear Portions of the Impregnation Curves for G30-500 Carbon Fiber Tows. .

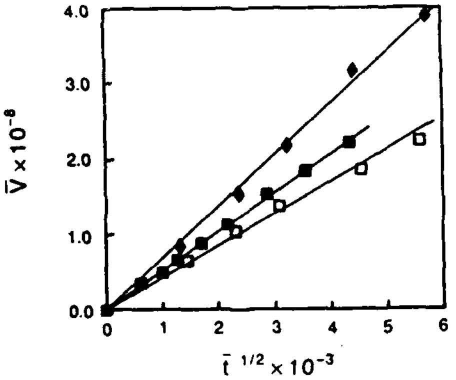

Note: Experiments 29 (■), 30 (◆), (θ = 0°) and the epoxy adhesive (□), (θ = 35°).

Figure 8. Linear Portion of the Impregnation Curve of T-1000B Carbon Fiber Tows.

The results of the experiments with different carbon fibers are given in Table 3. The AS4, G30-500, and T-1000 B fibers are more irregular in shape than the IM7 fibers. The general trend of increasing impregnation rates with larger porosities is discernible from the data. However, as in Table 2, at any given porosity, there are many impregnation rates. Experimentally, we have no control on the porosity and pore size distribution of the sample. Rather, they are measured during the impregnation experiments. Since the measurements of volume and, therefore, porosity are quite accurate, the multiplicity of rates at a given porosity is not an experimental artifact. Rather, it represents a need to characterize further the interstitial region of the tow experimentally and to develop further theories which will relate liquid uptake to the pore geometry.

Table 3. The Slope of the Linear Portion of Impregnation Curves for Different Carbon Fiber Tows Having Various Porosities

Run No.	CF	Porosity	Liquid	$\bar{A}$
10	AS4	45.8	10	0.83
11	AS4	53.6	10	1.17
12	AS4	56.5	100	0.69
13	AS4	57.5	500	0.85
14	AS4	60.8	100	0.83
15	AS4	64.3	10	1.16
16	AS4	64.6	500	1.16
17	AS4	65.5	100	1.06
18	AS4	69.5	100	1.24
19	G30-500	39.6	100	0.60
20	G30-500	39.8	100	0.47
21	G30-500	41.0	100	0.96
22	G30-500	42.9	10	0.56
23	G30-500	45.9	10	0.52
24	G30-500	49.9	10	1.15
25	G30-500	51.4	500	0.84
26	G30-500	53.1	500	1.02
27	G30-500	55.6	500	1.08
28	G30-500	56.2	500	1.03
29	T-1000B	49.7	500	1.07
30	T-1000B	56.3	10	1.44
31	IM7	38.4	100	0.56

For regular lattices, the axial impregnation rates for different pore models are shown in Figure 9. The experimental values of $\bar{A}$ calculated using Equation 18 for porosities from 0.24 to 0.65 are also given in Figure 9. Equation 8 gives the dependency of A_{hp} on porosity, when combined with Equation 4. The parameters $\bar{A}_1$ and $\bar{A}_2$ correspond to the rate constants associated with the pore radii r_1 and r_2 shown in Figure 1. They are calculated using Equations 2 and 3, with the definition of porosity. These experimental values are much higher than the theoretical ones based on regular lattice structures. Moreover, similar porosities can give rise to quite different experimental impregnation rates. However, for low porosities where the packing density and, hence, the regularity of the fiber geometry is high, the experimental rates are within the limits predicted by the simple theoretical models.

Cross-sectional views of epoxy-impregnated fiber bundles are shown in Figures 10 and 11. There are regions of high and low fiber density. There appears to be no microscopic voids in the tow (a conclusive statement requires the investigation of many cross sections of the tow; also, the polishing process might destroy voids). The scanning electron micrograph of the tow cross section shows that the fibers are indeed closely packed in the high density region (Figure 12). One can, therefore, postulate that the impregnation process is governed by fast vertical wicking in the large pores and a slow transverse penetration into the smaller pores (Bayramli and Powell 1990) which is coupled with axial flow in these small pores. Such a process would give rise to an apparent distribution of pore sizes, as shown in Figure 6.

5. CONCLUSION

These results show that even in the case of impregnation of a simple porous medium, such as fibers oriented parallel to their axes, the introduction of heterogeneity in the fiber-to-fiber separation creates a complicated flow which is very different from that in a perfectly regular matrix. The parameters defining the steady viscous flow are the porosity, the pore size distribution, and perhaps the contact angle. Making tensiometric measurements using porous carbon fiber tows allows the unambiguous determination of porosity and impregnation rates and, hence, makes it possible to elucidate the importance of these parameters in the impregnation process.

The expected linear relationship between the volume of liquid impregnated and the square root of the time is found for axially oriented fibers using liquids having contact angles of approximately zero and for

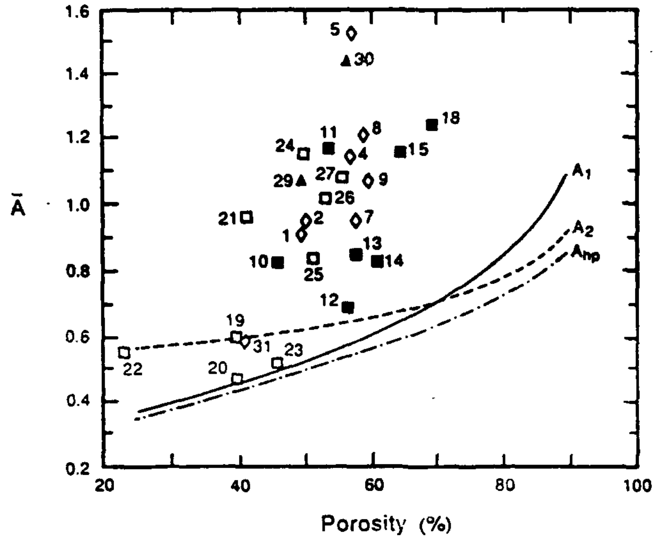

Note: The numbers denote the experiments in Tables 2 and 3: IM7 (◇); AS4 (■); G30-500 (□); T-1000B (▲). The theoretical lines are for A_1 and A_2, calculated assuming cylindrical capillaries with r_1 and r_2 (Figure 1), and for A_{hp} for the parallel plate hexagonal packing configuration.

Figure 9. Comparison of the Theoretical Dependence of $\bar{A}$ on Porosity for a Regular Hexagonal Lattice With the Experimentally Calculated Values.

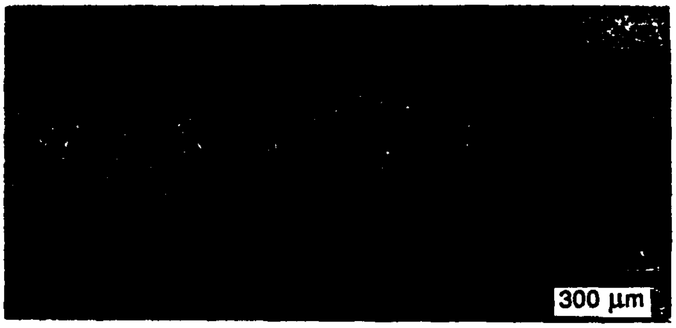

Note: The darkened boundary is the adhesive of the surrounding tape. The photograph is taken using an optical reflectance microscope. The bar denoted 300 µm.

Figure 10. Cross-Sectional View of the Epoxy-Impregnated IM7 Carbon Fiber Bundle.

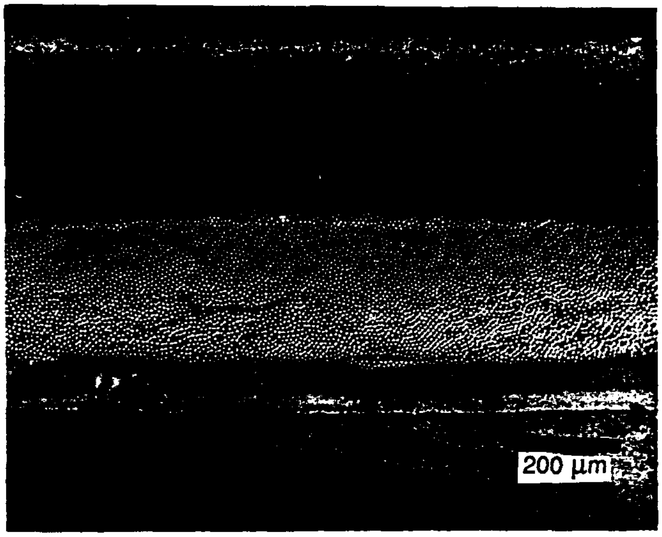

Note: The photograph is taken using an Optical Reflectance Microscopy. The bar denotes 200 µm.

Figure 11. Cross-Sectional View of the Epoxy-Impregnated G30-500 Carbon Fiber Bundle.

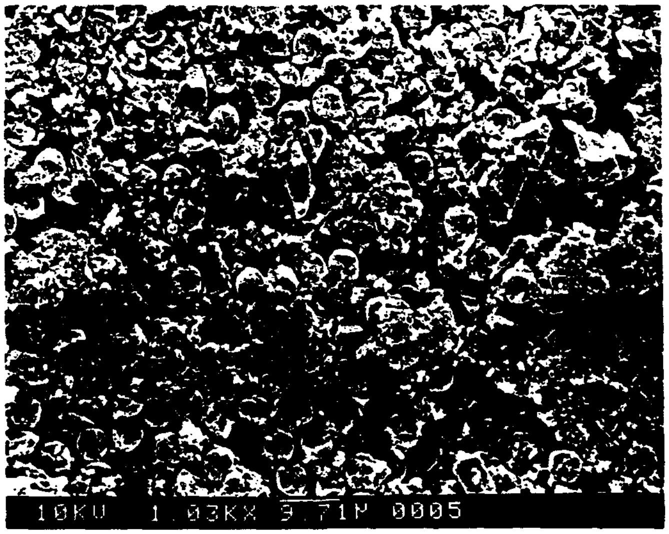

Note: The average fiber diameter is 5.0 µm. The bar at the bottom of the photograph denotes 9.7 µm.

Figure 12. Scanning Electron Micrograph of the Epoxy-Impregnated IM7 Carbon Fiber Bundle.

an uncured epoxy system with a finite contact angle. The observed rates of impregnation were sometimes over two times higher than those predicted from the average capillary dimensions (Figure 9). Furthermore, a multitude of impregnation rates is possible for a given average porosity, differing by as much as 50% in different experiments using different tow samples. Our conclusion is that the average porosity alone is not adequate to predict the wicking behavior. A knowledge of the pore size distribution is required for an accurate estimation of the impregnation rates.

A large heterogeneity in pore size distribution gives rise to faster rates of impregnation as compared with more homogeneous distributions. The observed rates of impregnation can be qualitatively explained by a fast uptake of liquids in the large pores coupled with lateral motion of the liquid into the neighboring smaller pores. It is likely that a more rigorous analysis of the impregnation process can be achieved by casting the problem in terms of Taylor-dispersion relationships (Brenner 1980) or more sophisticated models of the cell geometry (Levine and Neale 1975). In our case, the randomizing influence is the convoluted pore geometry in which there is a fast axial motion of the liquid in large pores together with an order of magnitude smaller motion in the small pores of the fiber matrix as well as lateral flow. In future work, we will aim at exploring this possibility.

Finally, the tensiometric technique (measuring the amount of impregnated liquid) and the analysis of the pore size distribution used in this study can be employed to characterize the structure of other types of porous material in terms of wicking or wetting behavior. Soil structures, solid porous catalysts, or woven fibers (Kim 1987) can be investigated with the preparation of suitable samples. Such studies may give clues as to the dimensional scaling of the porous materials.

6. REFERENCES

Bayramli, E., and R. L. Powell. Journal of Colloid Interface Science, vol. 138, p. 346, 1990.

Bayramli E., and R. L. Powell. To be published.

Brenner, H. Philos. Trans. Soc. London, Ser. A., vol. 297, p. 81, 1980.

Kim, J. Ph.D. Dissertation, Department of Chemical Engineering, Princeton University, Princeton, NJ, 1987.

Levine, S., and G. Neale. J. Chem Soc., Faraday Trans., vol. 2, no. 71, p. 12, 1975.

Lucas, R. Kolloid-Z, vol. 23, p. 15, 1918.

Morgan, R. J., F. M. Kong, and C. M. Walkup. Polymer, vol. 25, p. 375, 1984.

Okagawa, A., and S. G. Mason. Sixth Fundamental Research Symposium: Fibre-Water Interactions in Papermaking, Oxford, 1977. Technical Section, British Paper and Board Industry Federation, Oxford, pp. 581–586, 1978.

Princen, H. M. Journal of Colloid Interface Science, vol. 30, p. 359, 1969.

Washburn, E. W. Phys. Rev., vol. 17, p. 273, 1921.

INTENTIONALLY LEFT BLANK.

No. of Copies	Organization
2	Administrator Defense Technical Info Center ATTN: DTIC-DDA Cameron Station Alexandria, VA 22304-6145
1	Commander U.S. Army Materiel Command ATTN: AMCAM 5001 Eisenhower Ave. Alexandria, VA 22333-0001
1	Commander U.S. Army Laboratory Command ATTN: AMSLC-DL 2800 Powder Mill Rd. Adelphi, MD 20783-1145
2	Commander U.S. Army Armament Research, Development, and Engineering Center ATTN: SMCAR-IMI-I Picatinny Arsenal, NJ 07806-5000
2	Commander U.S. Army Armament Research, Development, and Engineering Center ATTN: SMCAR-TDC Picatinny Arsenal, NJ 07806-5000
1	Director Benet Weapons Laboratory U.S. Army Armament Research, Development, and Engineering Center ATTN: SMCAR-CCB-TL Watervliet, NY 12189-4050
(Unclass. only) 1	Commander U.S. Army Rock Island Arsenal ATTN: SMCRI-TL/Technical Library Rock Island, IL 61299-5000
1	Director U.S. Army Aviation Research and Technology Activity ATTN: SAVRT-R (Library) M/S 219-3 Ames Research Center Moffett Field, CA 94035-1000
1	Commander U.S. Army Missile Command ATTN: AMSMI-RD-CS-R (DOC) Redstone Arsenal, AL 35898-5010
1	Commander U.S. Army Tank-Automotive Command ATTN: ASQNC-TAC-DIT (Technical Information Center) Warren, MI 48397-5000
1	Director U.S. Army TRADOC Analysis Command ATTN: ATRC-WSR White Sands Missile Range, NM 88002-5502
1	Commandant U.S. Army Field Artillery School ATTN: ATSF-CSI Ft. Sill, OK 73503-5000
2	Commandant U.S. Army Infantry School ATTN: ATZB-SC, System Safety Fort Benning, GA 31903-5000
(Class. only) 1	Commandant U.S. Army Infantry School ATTN: ATSH-CD (Security Mgr.) Fort Benning, GA 31905-5660
(Unclass. only) 1	Commandant U.S. Army Infantry School ATTN: ATSH-CD-CSO-OR Fort Benning, GA 31905-5660
1	WL/MNOI Eglin AFB, FL 32542-5000
	Aberdeen Proving Ground
2	Dir, USAMSAA ATTN: AMXSY-D AMXSY-MP, H. Cohen
1	Cdr, USATECOM ATTN: AMSTE-TC
3	Cdr, CRDEC, AMCCOM ATTN: SMCCR-RSP-A SMCCR-MU SMCCR-MSI
1	Dir, VLAMO ATTN: AMSLC-VL-D
10	Dir, USABRL ATTN: SLCBR-DD-T

No. of Copies	Organization
11	Director Benet Weapons Laboratory U.S. Army Armament Research, Development, and Engineering Center ATTN: SMCAR-CCB, J. Keane T. Allen J. Vasilakis G. Friar J. Zweig L. Johnson T. Simkins V. Montvori J. Wrzochalski G. D'Andrea R. Hasenbein Watervliet, NY 12189
9	Commander U.S. Army Armament Research, Development, and Engineering Center ATTN: SMCAR-CCH-T, S. Musalli P. Christian K. Fehsal N. Krasnow R. Carr SMCAR-CCH-V, E. Fennell SMCAR-CCH, J. DeLorenzo SMCAR-CC, R. Price J. Hedderich Picatinny Arsenal, NJ 07806-5000
2	Commander U.S. Army Armament Research, Development, and Engineering Center ATTN: SMCAR-TD, V. Linder T. Davidson Picatinny Arsenal, NJ 07806-5000
1	Commander Production Base Modernization Activity U.S. Army Armament Research, Development, and Engineering Center ATTN: AMSMC-PBM-K Picatinny Arsenal, NJ 07806-5000
1	Commander U.S. Army Belvoir RD&E Center ATTN: STRBE-JBC, C. Kominos Fort Belvoir, VA 22060-5606
2	Commander U.S. Army Laboratory Command Harry Diamond Laboratories ATTN: SLCHD-TS-NT, A. Frydman 2800 Powder Mill Road Adelphi, MD 20783-1197
1	Commander U.S. Army Laboratory Command ATTN: AMSLC-TD, R. Vitali Adelphi, MD 20783-1145
1	Commander U.S. Army Missile Command ATTN: AMSMI-RD, W. McCorkle Redstone Arsenal, AL 35898
3	Commander U.S. Army Armament Research, Development, and Engineering Center ATTN: SMCAR-FSA-M, R. Botticelli F. Diorio SMCAR-FSA C. Spinelli Picatinny Arsenal, NJ 07806-5000
3	Project Manager Advanced Field Artillery System ATTN: COL Napoliello LTC D. Ellis G. DelCoco Picatinny Arsenal, NJ 07806-5000
1	Commander Watervliet Arsenal ATTN: SMCWV-QA-QS, K. Insco Watervliet, NY 12189-4050
2	Project Manager SADARM Picatinny Arsenal, NJ 07806-5000

No. of Copies	Organization
8	Project Manager Tank Main Armament Systems ATTN: SFAE-AR-TMA, COL Hartline SFAE-AR-TMA-MD, C. Kimker H. Yuen R. Joinson J. McGreen SFAE-AR-TMA-ME, K. Russell D. Guzowitz SFAE-AR-TMA-MP W. Lang Picatinny Arsenal, NJ 07806-5000
2	PEO-Armaments ATTN: SFAE-AR-PM, D. Adams T. McWilliams Picatinny Arsenal, NJ 07806-5000
2	Commander Wright-Patterson Air Force Base ATTN: AFWAML, J. Whitney R. Kim Dayton, OH 45433
1	Commander DARPA ATTN: J. Kelly 1400 Wilson Blvd. Arlington, VA 22209
2	Director U.S. Army Materials Technology Laboratory ATTN: SLCMT-MEC, B. Halpin T. Chou Watertown, MA 02172-0001
1	Naval Research Laboratory Code 6383 ATTN: Dr. I. Wolock Washington, DC 20375-5000
2	David Taylor Research Center ATTN: R. Rockwell W. Phyillaier Bethesda, MD 20054-5000
1	David Taylor Research Center Ship Structures and Protection Department Code 1702 ATTN: Dr. J. Corrado Bethesda, MD 20084
4	Director Lawrence Livermore National Laboratory ATTN: R. Christensen S. deTeresa W. Feng F. Magness P.O. Box 808 Livermore, CA 94550
2	Pacific Northwest Laboratory A Div of Battelle Memorial Inst. Technical Information Section ATTN: M. Smith M. Garnich P.O. Box 999 Richland, WA 99352
2	Director Sandia National Laboratories Applied Mechanics Department, Division-8241 ATTN: C. Robinson G. Benedetti P.O. Box 969 Livermore, CA 94550-0096
1	Director Los Alamos National Laboratory ATTN: D. Rabern MEE-13, Mail Stop J-576 P.O. Box 1633 Los Alamos, NM 87545

No. of Copies	Organization
3	University of Delaware Center for Composite Materials ATTN: J. Gillespe B. Pipes M. Santare 201 Spencer Laboratory Newark, DE 19716
2	North Carolina State University Civil Engineering Department ATTN: W. Rasdorf L. Spainhour P.O. Box 7908 Raleigh, NC 27696-7908
1	University of Utah Department of Mechanical and Industrial Engineering ATTN: S. Swanson Salt Lake City, UT 84112
1	Stanford University Department of Aeronautics and Aeroballisticss Durant Building ATTN: S. Tsai Stanford, CA 94305
1	Pennsylvania State University Department of Engineering Science and Mechanics ATTN: T. Hahn 227 Hammond Building University Park, PA 16802
1	University of Illinois at Urbana-Champaign National Center for Composite Materials Research 216 Talbot Laboratory ATTN: J. Economy 104 South Wright Street Urbana, IL 61801
1	University of Illinois at Urbana-Champaign Department of Aeronautical and Astonautical Engineering ATTN: A. Zak Urbana, IL 61801
2	Olin Corporation Flinchbaugh Division ATTN: E. Steiner B. Stewart P.O. Box 127 Red Lion, PA 17356
1	Olin Corporation ATTN: L. Whitmore 10101 9th St., North St. Petersburg, FL 33702
3	Alliant Techsystems, Inc. ATTN: C. Candland J. Bode K. Ward 5640 Smetana Dr. Minnetonka, MN 55343
1	Chamberlain Manufacturing Corporation Research and Development Division ATTN: T. Lynch 550 Esther Street P.O. Box 2335 Waterloo, IA 50704
1	Custom Analytical Engineering Systems, Inc. ATTN: A. Alexander Star Route, Box 4A Flintstone, MD 21530
2	Institute for Advanced Technology ATTN: T. Kiehne H. Fair 4030-2 W. Braker Lane Austin, TX 78759

USER EVALUATION SHEET/CHANGE OF ADDRESS

This laboratory undertakes a continuing effort to improve the quality of the reports it publishes. Your comments/answers below will aid us in our efforts.

1. Does this report satisfy a need? (Comment on purpose, related project, or other area of interest for which the report will be used.) ____________________

2. How, specifically, is the report being used? (Information source, design data, procedure, source of ideas, etc.) ____________________

3. Has the information in this report led to any quantitative savings as far as man-hours or dollars saved, operating costs avoided, or efficiencies achieved, etc? If so, please elaborate. ____________________

4. General Comments. What do you think should be changed to improve future reports? (Indicate changes to organization, technical content, format, etc.) ____________________

BRL Report Number BRL-CR-690 Division Symbol __________

Check here if desire to be removed from distribution list. ____

Check here for address change. ____

Current address: Organization ____________________

Address ____________________

DEPARTMENT OF THE ARMY
Director
U.S. Army Ballistic Research Laboratory
ATTN: SLCBR-DD-T
Aberdeen Proving Ground, MD 21005-5066

OFFICIAL BUSINESS

NO POSTAGE
NECESSARY
IF MAILED
IN THE
UNITED STATES

BUSINESS REPLY MAIL
FIRST CLASS PERMIT No 0001, APG, MD

Postage will be paid by addressee.

Director
U.S. Army Ballistic Research Laboratory
ATTN: SLCBR-DD-T
Aberdeen Proving Ground, MD 21005-5066